1   **High-resolution (1 km) Polar WRF output for 79°N Glacier and the Northeast of Greenland**
2   **from 2014-2018**

4   Jenny V. Turton[1], Thomas Mölg[1], Emily Collier[1]
5   [1]Climate System Research Group, Institute of Geography, Friedrich-Alexander University, Erlangen-
6   Nürnberg, 90158, Germany.
7
8   *Correspondence to:* Jenny V. Turton (jenny.turton@fau.de)

10   **Abstract**
11   **The northeast region of Greenland is of growing interest due to changes taking place on the**
12   **large marine-terminating glaciers which drain the north east Greenland ice stream.**
13   **Nioghalvfjerdsfjorden, or 79°N Glacier, is one of these that is currently experiencing**
14   **accelerated thinning, retreat and enhanced surface melt. Understanding both the influence of**
15   **atmospheric processes on the glacier and feedbacks from changing surface conditions is crucial**
16   **for our understanding of present stability and future change. However, relatively few studies**
17   **have focused on the atmospheric processes in this region, and even fewer have used high-**
18   **resolution modelling as a tool to address these research questions. Here we present a high**
19   **spatial- (1 km) and temporal- (up to hourly) resolution atmospheric modelling dataset,**
20   **NEGIS_WRF, for the 79°N and northeast Greenland region from 2014-2018, and an evaluation**
21   **of the model's success at representing daily near-surface meteorology when compared with**
22   **automatic weather station records. The dataset, (Turton et al, 2019b:**
23   **doi.org/10.17605/OSF.IO/53E6Z), is now available for a wide variety of applications in the**
24   **atmospheric, hydrological and oceanic sciences in the study region.**

25

26   **1. Introduction**
27   The surface mass balance of a glacier is largely controlled by regional climate through varying mass
28   gains and losses in the ablation and accumulation zones, respectively. The large amount of mass lost
29   from the Greenland Ice Sheet (GrIS) within the last few decades (approximately 3800 billion tonnes of
30   ice between 1992 and 2018: Shepherd et al., 2020) has largely been located around the coast of
31   Greenland, due to the thinning and retreat of marine-terminating glaciers (Howat & Eddy, 2011), and
32   the surface mass loss in the ablation zone due to enhanced melting and runoff (Rignot, et al., 2015;
33   van den Broeke et al., 2017). A recent study found that enhanced meltwater run off, connected to
34   changing atmospheric conditions, was the largest contributor of mass loss for Greenland (52%)
35   (Shepherd et al., 2020). The remaining 48% of mass loss (1.8 billion tonnes of ice) was due to
36   enhanced glacier discharge, which has been increasing over time (Shepherd et al., 2020).

37   The majority of studies of the surface mass loss in Greenland and its atmospheric controls are
38 largely constrained to southern and western Greenland (e.g Kuipers Munneke et al., 2018; Mernild et
39 al., 2018), or to specific warm events such as the 2012 melt event (e.g Bennartz et al., 2013; Tedesco
40 et al., 2013). However, recent studies have shown that the northeast of Greenland, specifically the
41 North East Greenland Ice Steam (NEGIS) is now experiencing high ice velocity and accelerated
42 thinning rates (Joughin et al., 2010; Khan et al., 2014). NEGIS extends into the interior of the
43 Greenland ice stream by 600 km and three marine-terminating glaciers connect the NEGIS with the
44 ocean. The largest of these glaciers is Nioghalvfjerdsfjorden, often named 79°N after its latitudinal
45 position. Until recently, very few studies focused on 79°N glacier and NEGIS as they were thought to
46 contribute little to surface mass loss and instabilities (Khan et al., 2014; Mayer et al., 2018). However,
47 79°N glacier, with its 80 km long by 20 km wide floating tongue, has retreated by 2-3 km between
48 2009 and 2012, and the surface of the tongue and part of the grounded section of the glacier are now
49 thinning at a rate of 1 m yr^{-1} (Khan et al., 2014, Mayer et al. 2018). The glacier is at a crucial
50 interface between a warming ocean and a changing atmosphere. The mass loss from the floating
51 tongue is largely attributed to basal melting due to the presence of warm (1°C) ocean water in the
52 cavity below the glacier (Wilson & Straneo, 2015, Schaffer et al., 2017, Münchow et al., 2020).
53 However, even the grounded part of the glacier is characterised by large melt ponds and drainage
54 systems (Hochreuther, P. pers. comm); suggesting that atmospheric processes may also be at play.
55 Furthermore, atmospheric processes may be responsible for driving the warm Atlantic water under the
56 glacier tongue, which leads to melting of the glacier base (Münchow et al., 2020). 79°N glacier is of
57 further interest because its southerly neighbour, Zachariae Istrom, recently lost its floating tongue
58 (Mouginot et al., 2015).
59   A number of studies have used atmospheric modelling as a tool to investigate the region,
60 although they have largely been confined to short case studies (Turton et al., 2019a), focused on past
61 climates (e.g 45000 years ago by Larsen et al., 2018), or targeted specific atmospheric processes
62 (Leeson, et al., 2018; Turton et al., 2019a). There are a number of atmospheric models that have
63 been applied to the Greenland region, however these are often run at a resolution that is too coarse to
64 resolve the 79°N glacier, especially its floating tongue, which can therefore be missing in many
65 simulations. These data are usually statistically downscaled to calculate the surface mass balance of the
66 glacier, using a digital elevation model and a shape file of the glacier. The resolution of the
67 atmospheric models used in published studies for Greenland generally exceed 10km: e.g the Modèle
68 Atmosphérique Régional (MAR) at 20-km (Fettweis et al, 2017) RACMO2 at 11-km (Noël et al.,
69 2016) and HIRHAM5 at 25-km (Mottram et al., 2017a). Recently, there have been attempts at
70 modelling the polar regions using non-hydrostatic regional climate models, including HARMONIE-
71 AROME at 2 km resolution for the Southwest of Greenland (Mottram et al., 2017b), and the NHM-
72 SMAP at 5 km resolution for the whole of Greenland (Niwano et al., 2018). However, the Mottram et

73   al. (2017b) study does not include the northeast of Greenland. Furthermore, the focus of the Niwano

74   et al. (2018) study was to improve the surface mass balance estimates, as opposed to providing output

75   for a more general atmospheric sense, and the model was not convection permitting. In convection-

76   permitting models, typically for spatial resolutions higher than 5km, convection begins to be

77   explicitly resolved. This can enhance the representation of convection and associated precipitation, as

78   opposed to using a convection parameterisation scheme, (Pal et al., 2019). As yet, there are no very

79   high-resolution, multi-year atmospheric datasets available for the northeast of Greenland or the wider

80   region.

81   Here, we address this data gap by presenting a 5-year (2014-2018), high-resolution (1 km)

82   atmospheric simulation using a polar-optimised atmospheric model and evaluate its skill in

83   representing local meteorological conditions over the 79°N region in northeast Greenland. The dataset

84   is named NEGIS_WRF after its location of focus and model used. As the 79°N region is of growing

85   interest, this data could be beneficial for numerous other studies and applications. Indeed, current

86   ongoing research as part of the Greenland Ice sheet-Ocean interaction (GROCE) project

87   (www.groce.de, last accessed October 1 2019) include using this data for surface mass balance studies

88   and to investigate the relationship between specific atmospheric processes and surface melt patterns.

89   For studies of the surface mass balance of the NEGIS, further downscaling would not be necessary.

90   With a horizontal resolution of less than 5km, many atmospheric processes are accurately resolved

91   including katabatic winds and warm-air advection (Turton et al., 2019a). Furthermore, high-resolution

92   output is crucial for the complex topography on the northeast coast, where steep and variable

93   topography can channel or block the winds, and lead to strong variability of the radiation budget. The

94   WRF dataset is also intended as input to an ocean model, used in an ocean-glacier interaction study,

95   input into a hydrologic model and for an ice sheet modelling study. Here we present an evaluation of

96   the ability of NEGIS_WRF at representing key near-surface meteorological and radiative conditions,

97   to demonstrate the applicability of the dataset for these and other studies in the atmospheric,

98   cryospheric and oceanic fields.

99

100   **2. Data and Methods**

101   **2.1 Model Configuration**

102   The Polar Weather Research and Forecasting (Polar WRF) model is a version of the WRF

103   model that was developed and optimised for use in polar climates (Hines et al., 2011). The non-

104   hydrostatic WRF model (available online from http://www.mmm.ucar.edu/weather-research-and-

105   forecasting-model; last accessed July 29 2019) has been widely used for both operational studies

106   and for research in many regions, and at many scales (Powers et al., 2017; Skamarock & Klemp,

107   2008). The current version of polar WRF used here is v3.9.1.1, which was released in January 2018,

108   and is available from http://polarmet.osu.edu/PWRF/ (last accessed July 29 2019). Polar WRF has

109   been developed for use in the Arctic and Antarctic by largely optimising the Noah Land Surface Model

110   (LSM) (Chen & Dudhia, 2001) to improve heat transfer processes through snow and permanent ice,

111   and by providing additional methods for sea-ice treatment (Hines et al, 2015). For a full description of

112   the Polar WRF additions, see (Hines & Bromwich, 2008; Hines et al., 2011; Hines et al., 2015) and

113   citations therein.
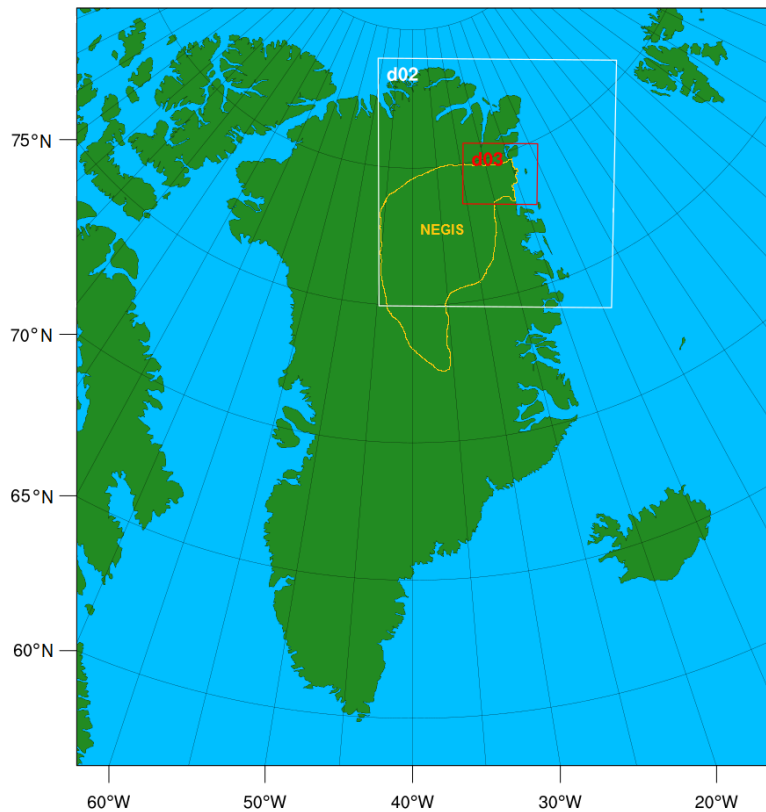
114

115   **Figure 1: The domain configuration for the Polar WRF runs and the approximate outline of**

116   **NEGIS following Khan et al. (2014).**

117

118   The meteorological initialisation and boundary input data is from the ECMWF (European

119   Centre for Medium range Weather Forecast) ERA-Interim dataset at 6-hourly intervals (Dee et al.,

120   2011). This reanalysis product was more accurate at resolving mesoscale processes in the northeast of

121   Greenland compared to MERRA2 reanalysis data and has previously been used for Polar WRF

122   simulations in Greenland (DuVivier & Cassano, 2013; Turton et al., 2019a). The Sea Surface

123   Temperature (SST) and sea ice concentration values are from the NOAA Optimum Interpolation

124   0.25° resolution daily data. This is a combination of data from the Advanced Very High Resolution

125   Radiometer (AVHRR) infrared satellite and Advanced Microwave Scanning Radiometer (AMSR)

126   (doi:10.5065/EMOT-1D34, data retrieved from https://rda.ucar.edu/datasets/ds277.7/, last accessed

127   July 29 2019). In-situ ship and buoy data are used to correct satellite biases, leading to relatively low

128   mean biases of 0.2-0.4K for SST data (more information on this dataset can be found in Banzon et al.,

129   2016). This higher resolution dataset was required due to the very blocky coastline in the SST and sea

130   ice data from ERA-Interim. The domain setup is shown in Figure 1. The outermost domain (D01) is at

131   25km, D02 is 5km and D03 (innermost) is 1km grid spacing. Boundary conditions, including sea ice

132   fraction and SST were updated every 6-hours. Analysis nudging was used in the outer domain (D01)

133   to constrain the large-scale circulation while allowing the model to freely simulate in D02 and D03.

134   Nudging is the process of constraining the interior of model domains towards the larger-scale field

135   (from reanalysis data) which drive the simulation (Lo et al., 2008., Otte et al., 2012). It has been

136   found to improve simulations of the large-scale circulation (Bowden et al., 2012) and reduce errors in

137   the mean and extreme values (Otte et al., 2012) from relatively long runs. We only nudge the outer

138   domain (D01) to allow the higher-resolution domain to evolve freely. The USGS 24 category landuse

139   and landmask was adjusted using the European Space Agency (ESA) Climate Change Initiative (CCI)

140   landuse product, to provide a better representation of the glacier outlines and the terminus of the

141   floating tongue (https://www.esa-landcover-cci.org/, last accessed September 5 2019). A number of

142   open-water grid points were manually changed to glacierised during January-June and September-

143   December to better represent the floating tongue of the Spalte Glacier (tributary of 79°N on the

144   northeast side) and the sea ice in the adjacent Dijmphna Sound (Fig. 2). Other small exposed water

145   areas along the coast, which are permanently frozen except in July and August each year

146   (Hochreuther, P., 2019 personal communication), were also changed to ice during all months except

147   July and August (Fig. 2). The glacier extents are treated as static throughout the run, which is an

148   appropriate approximation given the small and likely negligible area of calving of 79°N during our

149   study period (see ENVEO, 2019 for calving front locations from 1990 to 2017). There are 60 levels in

150   the vertical, with a 10-hPa model top and a lowest model level ~16m above the surface.

151   Many of the parameterisations for the model configuration were selected based on numerous,

152   previous Polar WRF runs over Greenland and the Arctic (for example Hines et al., 2011). In brief, the

153   following parameterisations were employed: the Noah LSM (Chen & Dudhia, 2011), due to its

154   optimisations that have been tested over Greenland (Hines & Bromwich, 2008), Arctic sea ice (Hines,

155   et al 2015) and Arctic land (Hines et al., 2011); the Morrison two-moment scheme for microphysics,

156   which has been shown to out-perform other schemes in both Polar regions (Bromwich, et al., 2009;

157   Lachlan-Cope, et al., 2016; Listowski & Lachlan-Cope, 2017); the Eta Similarity Scheme for surface

158   layer physics (Janjić, 1994) and the Yonsei University Scheme for planetary boundary layer

159   parameterisation. This was used due to the topographic wind scheme (Hong et al., 2006) that can

160   correct excessive wind speeds in areas of complex topography, such as the northeast coast of

161   Greenland (employed in D02 and D03 only, where complex orography is best resolved). Further

162   parameterisations include: the Kain-Fritsch scheme for cumulus convection (Kain, 2004) (D01 and

163   D02 only, as the resolution of D03 allows convection to be explicitly resolved); and, the Rapid

164   Radiative Transfer Model (RRTM) longwave and Goddard shortwave schemes for radiation, based

165   on sensitivity testing for the polar regions by Hines et al. (2008) and subsequent runs over Greenland

166   (DuVivier & Cassano, 2013; Hines et al., 2011). Whilst the majority of these options were selected

167 for testing based on the works of other publications, a short sensitivity study was also conducted,
168 alongside with testing the horizontal and vertical resolution and locations of the domains (not
169 included). It was found that a combination of the options above were best suited to the northeast of
170 Greenland when compared with observations on the floating tongue of the 79°N glacier from 1996-
171 1999 (Turton et al., 2019a).
172   Other options specified for this study include using a fractional sea ice treatment, which
173 allows calculation of different surface temperature, surface roughness and turbulent fluxes for open
174 water and sea ice conditions within the grid cell, and then calculates an area-weighted average for the
175 grid (DuVivier & Cassano, 2013; Hines et al., 2011). The adaptive timestep was used to optimise the
176 simulation speed. For each year simulated, the model was initialised on September 1 before the onset of
177 the accumulation season and ran continuously until October 1 of the following year (e.g September 1
178 2016 - October 1 2017). September was then discarded as a spin up month. The model produces
179 similar magnitude snow depths to available observations (Pedersen et al. 2016). Due to limited
180 snowfall and snow depth observations in this region, we compared cumulative snowfall to ERA5
181 products during testing, which have been shown to have a relatively good agreement with
182 observations by Wang et al. (2019). The maximum snow depth and average annual accumulation
183 were well captured by Polar WRF compared to ERA5.
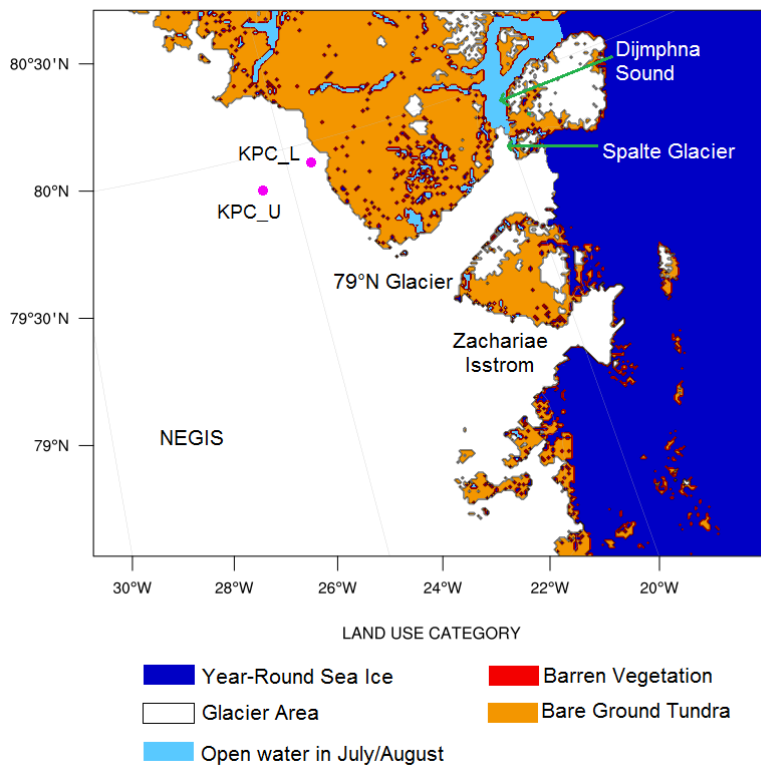
184
185 **Figure 2: A map of the land use types for D03. Colours represent the land use type, except for**
186 **light blue, which highlights the manually changed land use from open water to sea ice during**

187 **winter. Important locations are also highlighted, as are the locations of the two AWS sites (pink**

188 **dots).**

189

190 The data were output at hourly intervals for D03, at six-hourly intervals for D02 and at daily intervals

191 for D01. Daily mean values for key meteorological variables from D02 and D03 were calculated from

192 the hourly values and are available along with the daily instantaneous values from D01 at the Open

193 Science Framework repository (Turton et al. 2019b: doi.org/10.17605/OSF.IO/53E6Z).

194

195 **2.2 Observational Data**

196 The remote nature of the location of interest provides few in-situ observational datasets for model

197 evaluation. However, the PROMICE (Programme for Monitoring of the Greenland Ice Sheet) network

198 (www.promice.dk, last accessed October 1 2019; van As & Fausto, 2011), operated by the Geological

199 Survey of Denmark and Greenland (GEUS) has two permanent Automatic Weather Stations (AWSs)

200 available for comparison of daily means of meteorological variables and a number of surface energy

201 balance components. The AWSs are referred to as KPC_L and KPC_U due to their location on

202 Kronprincs Christian Land (located to the northwest of 79°N glacier; see Table 1 for AWS details of

203 location, dates and available variables. Although hourly data are available, daily means are used for

204 evaluation due to the multi-year timescale of the study, but the authors note that an evaluation of

205 hourly data should be performed before using these data for analysis at these time scales. Please refer

206 to van As & Fausto, (2011) and Turton et al., (2019a) for more information on the PROMICE data in

207 this location (doi.org/10.22008/promice/data/aws, available at www.promice.dk, last accessed

208 October 1 2019). Observations are not taken at exactly 2m above the surface but vary with

209 accumulation and ablation. Over bare ice, the sensor is 2.6m above the surface (van As et al., 2011).

210 To clarify that the observations represent near-surface conditions, and are compared with 2m and 10m

211 model output, we use the abbreviation X2 or X10 to represent both modelled and observed variables

212 at the respective heights. The mean values from the observational data are calculated from daily

213 averages from January 1 2014- December 31 2018 to keep a consistent period across all data.

214 The in-situ AWS observational data are used to evaluate the NEGIS_WRF output and to

215 provide a judgement of its skill to benefit future users. The focus of the evaluation is to test WRF's

216 ability to represent local meteorological conditions over a polar glacier. Daily mean values from

217 NEGIS_WRF have been calculated from hourly output at the location of the two AWSs. All

218 evaluation focuses on near-surface meteorological output from D03.

219

220 **Table 1: The location, elevation and data availability of the two AWSs used for model**

221 **evaluation. We evaluate the model output with four variables from the AWSs. Data was**

222 **unavailable at KPC_L between January 15 2010 and July 17 2012 due to retrieval problems. T**

223 **is air temperature, Q is specific humidity, WS and WD are wind speed and direction,**

respectively. Observations are taken at approximately 2m above the surface, but this does vary

224

with accumulation and ablation (see section 2.2). Sensor error estimates come from the sensor

225

manufacturers. See van As & Fausto (2011) for more information on sensors and observations.

226

Name	Location	Elevation (m a.s.l)	Data Availability	Variables used for evaluation	Sensor Error Estimates
KPC_L	79.91°N, 24.08°W	380	01.01.2009- present	T, Q, WS, WD, SW$_{down}$, LW$_{down}$	T: ± 0.2°C RH: ± 1.5% WS: ± 0.3ms^{-1} WD: ± 3° Radiation: 10%
KPC_U	79.83°N, 25.17°W	870	01.01.2009- 14.01.2010, 18.07.2012-present	T, Q, WS, WD, SW$_{down}$, LW$_{down}$	T: ± 0.2°C RH: ± 1.5% WS: ± 0.3ms^{-1} WD: ± 3° Radiation: 10%

227

228 **3. Results**

229 **3.1 Model evaluation: Daily Means**

230 The air temperature is simulated well by the WRF simulations with a coefficient of determination (R^2)

231 of 0.92 at both KPC_L and KPC_U (Table 2, Fig 3). Similarly, the mean biases and RMSE are small.

232 The mean bias and RMSE are slightly larger during winter (DJF) at KPC_U, but overall, the R^2 value

233 at both locations remains above 0.64. The particularly low daily temperatures observed during winter

234 at KPC_U are not fully captured by the WRF simulations (Fig. 3b). The model can, however, capture

235 the larger variability in winter (Fig. 3), including 'warm-air events', where the air temperature

236 increases by more than 10°C in a few days, leading to temperatures above the average for winter

237 (Turton et al., 2019a). Figure 4 presents the near-surface air temperature and 10m wind vectors for

238 June 6 2015, to show what the temperature and wind fields look like for an example time period

239 during the ablation period (June to August). The onset of the ablation season is earlier over the

240 floating tongue of the glacier, as seen by the above freezing air temperatures at low elevations in

241 Figure 4. WRF simulates the humidity very well annually and during winter for both locations. The

242 humidity during summer is slightly less well simulated, with mean biases of 0.4 and 0.6 g/kg for

243 KPC_L and KPC_U respectively (Table 2). However, the R^2 values remain above 0.44 for the

244 summer season. For both locations, annually and seasonally, WRF is moister than in observations,

245 however the mean biases remain relatively small (less than 0.6 g/kg), and the differences are not

246 statistically significant except for during summer at KPC_U (which is statistically different at the 99%

247 confidence level using a student t-test). The wind direction in WRF deviates more from the AWS data

248 than for temperature and moisture, which is likely due to the particularly steep and complex

249 topography of the region which may not be accurately represented by the model, even at 1 km

250 resolution. The largest bias is an annual bias at KPC_L (10.7°) as WRF simulates the wind direction

251 predominantly more northerly than in observations (Table 2), which leads to poor R^2 values (0.01) and

252 high RMSE. For KPC_U annually and seasonally, the biases remain at or below 8.6° and R^2 values

253 are 0.36, which shows that WRF is capable of representing the wind direction at KPC_U. Some of

254 these errors may relate to measurement errors of the wind senor, which is ±3° (see Table 1). The

255 model performs better at simulating the wind speed than the wind direction. Annually and during

256 winter, the R^2 values are relatively high (above 0.31) at both locations, and mean biases remain at or

257 below 2.3 ms^{-1} both annually and seasonally. None of the biases between WRF and observations are

258 statistically significantly different for daily mean wind speed or air temperature (Table 2).

259   Shortwave and longwave radiation values are important for a range of possible future studies

260 including input to surface mass balance and ocean models. Therefore, we have validated the

261 NEGIS_WRF output for both the downwelling shortwave and longwave by comparing it to

262 observations at the two sites (Table 2). Annually, the biases are within sensor error range (Table 1)

263 and differences between WRF and observations are not statistically significant for both downwelling

264 shortwave (SW_{down}) and longwave (LW_{down}). Due to the lack of sunlight during winter at this latitude,

265 the SW_{down} biases and RMSE are small and the R^2 values (0.78 and 0.75 for KPC_L and KPC_U

266 respectively) are high for both locations (Table 2). The mean biases are largest for SW_{down} during

267 summer, but a relatively high R^2 value shows that WRF still has a great deal of skill (0.82 at KPC_U).

268 Biases for LW_{down} are largest during winter (-10.3 and -15.3 Wm^{-2} at KPC_L and KPC_U

269 respectively), which is likely a product of increased wintertime variability due to storm frequency and

270 location (van As et al., 2009). Similarly, Cho et al. (2020) found that biases of LW_{down} compared to

271 satellite observations were larger for the Morrison microphysics scheme (which we use here) than for

272 the WRF single moment 6-class scheme. However, it was concluded that Polar WRF has the ability to

273 accurately simulate the spatial distribution of Arctic clouds and their optical properties with both

274 tested schemes (Cho et al., 2020). None of the differences between WRF output and observations for

275 the radiation components were statistically significant (Table 2).

276

277 **Table 2: Comparison of the near-surface WRF model output to AWS data at KPC_L and**

278 **KPC_U. ANN refers to annual mean values, DJF refers to winter average values whereas JJA**

279 **refers to summer average values. * refers to statistically significant differences between WRF**

280 **and AWS at the 99% confidence interval, using the student's t-test.**

Variable (units)	Location	AWS Mean	Mean Bias	RMSE	R^2

			(WRF-AWS)		
T2 ANN (°C)	KPC_L	-13.6	-0.3	3.0	0.92
	KPC_U	-17.2	1.8	4.0	0.92
T2 DJF (°C)	KPC_L	-23.3	0.0	3.2	0.86
	KPC_U	-27.6	2.6	5.2	0.64
T2 JJA (°C)	KPC_L	1.6	-1.8	2.6	0.71
	KPC_U	-1.5	-0.1	1.9	0.69
Q2 ANN (g/kg)	KPC_L	1.6	0.2	0.4	0.92
	KPC_U	1.4	0.3	0.5	0.92
Q2 DJF (g/kg)	KPC_L	0.4	0.1	0.1	0.81
	KPC_U	0.3	0.1	0.2	0.66
Q2 JJA (g/kg)	KPC_L	3.2	0.4	0.8	0.44
	KPC_U	3.0	0.6*	0.9	0.56
WD10 ANN (°)	KPC_L	219.4	10.7*	74.3	0.01
	KPC_U	277.9	3.4	29.9	0.36
WD10 DJF (°)	KPC_L	238.5	-3.2	49.9	0.01
	KPC_U	274	8.6	29.1	0.36
WD10 JJA (°)	KPC_L	211.6	6.8*	80.2	0.01
	KPC_U	279.9	-0.1	31.7	0.25
WS10 ANN (m/s)	KPC_L	5.7	0.4	2.9	0.42
	KPC'_U	4.8	1.5	2.5	0.49
WS10 DJF (m/s)	KPC_L	6.4	1.0	3.2	0.50
	KPC_U	5.2	2.3	3.4	0.38
WS10 JJA (m/s)	KPC_L	5.4	-0.8	2.7	0.31
	KPC_U	4.2	0.8	1.9	0.45
SW_{down} ANN (Wm^{-2})	KPC_L	114.5	4.7	34.1	0.94
	KPC_U	124.6	3.8	23.8	0.97
SW_{down} DJF (Wm^{-2})	KPC_L	0.1	-0.1	0.4	0.78
	KPC_U	0.2	-0.1	0.5	0.75
SW_{down} JJA (Wm^{-2})	KPC_L	271.6	13.1	62.3	0.63
	KPC_U	295.1	11.9	42.2	0.82
LW_{down} ANN (Wm^{-2})	KPC_L	212.0	-7.1	24.7	0.76
	KPC_U	202.5	-9.2	26.1	0.71
LW_{down} DJF (Wm^{-2})	KPC_L	181.9	-10.3	26.8	0.50
	KPC_U	179.6	-15.3	31.6	0.40

LW$_{down}$ JJA (Wm^{-2})	KPC_L	267.3	-4.9	23.8	0.38
	KPC_U	250.8	-6.4	21-6	0.49

281

282 The larger RMSE and lower R^2 values during summer for wind direction can, at least partly, be

283 attributed to the larger variability of those variables during summer. In summer (JJA), the average

284 deviation of wind direction in observations at KPC_L is 40.3°. Whilst WRF is able to capture this

285 variability in wind direction (the average deviation is 41.1°), there is sometimes an offset in the timing

286 of the wind direction change between WRF and observations. For example, after two weeks of

287 consistently northwesterly winds being observed at KPC_L between August 11 to 24, 2014, there was

288 a shift to northeasterly flow on the morning of August 25 2014 (Fig 5e). WRF successfully simulated

289 the long period of northwesterly winds, and the shift to winds from the northeast, however the change

290 in direction was simulated in the late evening of August 25 to early morning of August 26 (Fig. 5f),

291 leading to a bias of 156.9° on August 25. The northeasterly wind was only observed for 24 hours

292 before returning to westerly on August 26 (Fig. 5g). WRF was able to capture the short-lived timing

293 of the event, but 24 hours later. In this particular case, the wind direction error comes from the

294 boundary data, ERA-Interim. In ERA-Interim, the wind direction change starts on August 24 but

295 remains northerly until 18:00 UTC on August 25. It then remains northeasterly until August 27, which

296 is 24-hours longer than in near-surface observations. The later onset and more persistent flow from the

297 northeast in ERA-Interim likely led to the later onset of northeasterly flow in WRF. Therefore, WRF

298 can capture both the predominant wind flow, and abrupt changes to the wind direction, along with

299 capturing even short-lived events, although the timing is occasionally shifted. Figure 5 also highlights

300 that whilst the annual mean bias for wind speed is less than 1.5 ms^{-1} (Table 2), during certain periods,

301 WRF simulates higher wind speeds than observed. However, these are not unrealistic values for this

302 region, with a maximum observed wind speed of 20.2 ms^{-1} and a maximum simulated wind speed of

303 22.3 ms^{-1} for the KPCL location. The largest values and biases of wind speed occur during

304 particularly strong katabatic events (northwesterly wind direction during winter). This was also found

305 by Hines & Bromwich (2008) when using the same land surface scheme as in these simulations.

306 Overall, WRF performs well at simulating air temperature, humidity, downwelling radiation

307 and wind speed during the simulation period (Oct 2013 - Dec 2018). WRF struggles to as accurately

308 represent the wind direction, especially at KPC_L (which is likely due to the proximity of complex

309 topography to the KPC_L site), however the winds remain predominantly westerly to northwesterly,

310 which shows that WRF can capture the dominant katabatic process governing the wind directions.

311
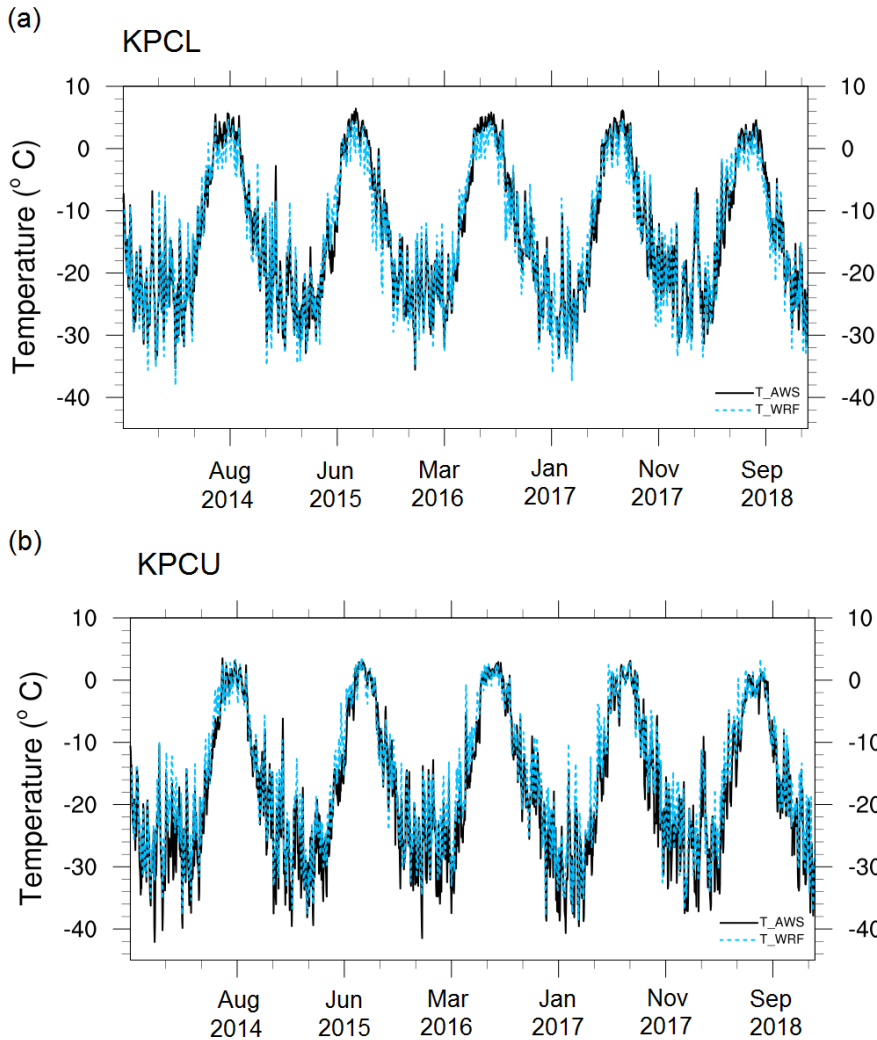
Figure 3: The observed (black lines) and modelled (dashed blue lines) daily average air temperature at KPC_L (top) and KPC_U (bottom) from D03.

314

3.2 Model evaluation: Sub-daily Data

To evaluate the ability of the model to simulate sub-daily values, the minimum and maximum daily near-surface values (from hourly output) are compared to observations, and the amplitude of the diurnal cycle of air temperature is also evaluated. Figure 6 presents the statistics for daily minimum and maximum air temperatures at the two locations in observations and WRF. The median values are well captured by WRF, especially for the maximum daily values, where a median value of -13.9°C is observed at KPC_U, and -14.0°C is simulated. Similarly, for maximum temperatures, the 75th quartile values are well captured by WRF (Fig. 6). For KPC_L, the minimum and maximum temperatures are colder in WRF than in observations. For example, the 25th percentile value for the minimum temperatures (far left bar in Fig. 6) is 3.8°C in observations, but 6.3°C in WRF. At KPC_U, the

325 opposite is true, where WRF simulates slightly higher temperatures than in observations. However,

326 overall, the range of minimum and maximum temperature values are well modelled by WRF.

327 The average daily maximum air temperature observed at KPC_L is -21.0°C in winter (DJF)

328 and increases to 3.0°C in summer (JJA). WRF simulates an average daily maximum of -20.9°C in

329 winter, which increases to 0.9°C in summer. The average daily minimum air temperature observed at

330 KPC_L is –25.9°C during winter and rises to 0.2°C in summer. WRF simulates an average daily

331 minimum air temperature of -26.5°C in winter and increasing to -2.3°C in summer. Therefore, WRF is

332 able to accurately simulate the winter minimum and maximum temperatures. WRF slightly

333 underestimates the air temperature during summer, however at KPC_U, this is within the error

334 estimate provided by the sensor manufacturer (Table 1), and for both locations the biases are not

335 statistically significant (Table 2).

336 Similarly, at KPC_U, the observed maximum temperature values are -24.1°C in winter and

337 0.1°C in summer. From WRF, the average maximum temperature is -22.5°C in winter and increases

338 to -0.1°C in summer. The observed minimum daily air temperature at KPC_U is -30.8°C during

339 winter and –3.5°C in summer. In comparison, in the WRF simulations, the average daily minimum

340 temperature is -27.4°C during winter and increases to -3.9°C in summer. WRF can therefore represent

341 the maximum and minimum daily air temperatures at KPC_U.

342 The annual-average observed diurnal air temperature amplitude is 5.6°C at KPC_U and 4.0°C

343 at KPC_L. The largest average diurnal cycle is observed during spring (MAM) at KPC_U (6.8°C) and

344 during winter at KPC_L (4.9°C). The WRF model simulated an average diurnal amplitude of 5.0°C at

345 KPC_U 4.7°C at KPC_L. The largest diurnal cycles are simulated during spring at KPC_U (6.2°C)

346 and during winter at KPC_L (5.5°C). Therefore, WRF accurately simulates the timing of the largest

347 diurnal amplitudes but overestimates the amplitude slightly at KPC_L, and underestimates it at

348 KPC_U, both by 0.6°C. The relatively large diurnal amplitude in winter may be counterintuitive given

349 that the glacier is located in the Arctic, where polar night (no solar radiation) prevails throughout

350 winter. However, the temperature variability is largest during winter over the glacier due to the more

351 frequent passing of storms across the Atlantic Ocean and the occurrence of 'warm-air events' from

352 easterly horizontal advection and increased longwave radiation from clouds (van As et al. 2009,

353 Turton et al. 2019a). Warm-air events are characterised by large (>10°C) temperature increases

354 between November and March, which can last for a number of days and, on average, occur 10 times

355 per year (standard deviation of 4.0) (Turton et al., 2019a). The variability can be further enhanced by

356 turbulent mixing from katabatic winds and the presence of föhn winds (Turton et al., 2019a).
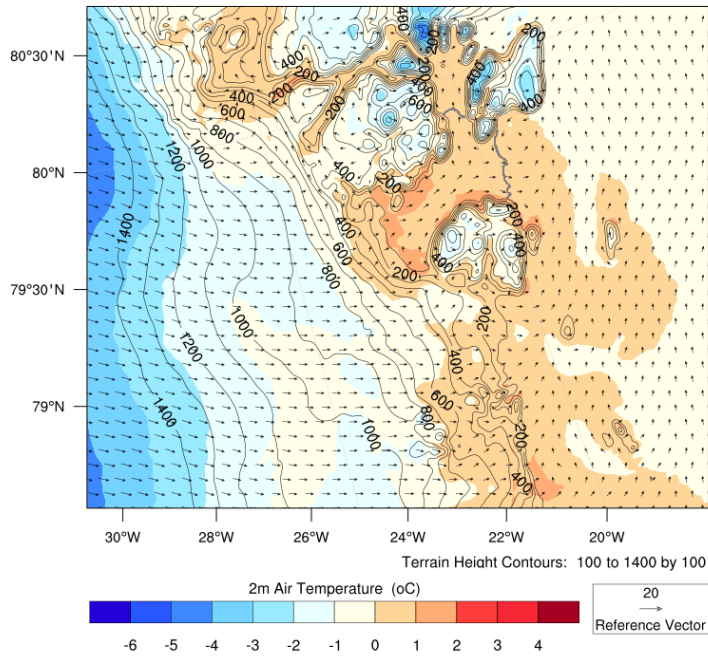
Figure 4: The 2m air temperature (colours), wind vectors (arrows) and terrain height contours (black lines) for June 6 2015. The edge of 79°N glacier is shown by the dark grey line.

The maximum hourly air temperature over the four years of data observed at KPC_L was on July 23, 2014 (8.1°C) (Fig. 6). WRF was able to replicate the processes responsible for the particularly warm day, as a daily maximum value of 4.5°C was modelled at KPC_U. At KPC_L, the maximum was simulated 24-hours earlier (6.5°C). The maximum values from WRF are slightly lower than observed (Fig. 6), but the timing of the maximum was accurate. The lower maximum values are likely linked to the negative mean bias in temperature simulated by WRF during the summer months (Table 2).

The absolute minimum hourly air temperature was observed at KPC_U on December 26, 2015 (-45.0°C) (Fig. 6) and on December 27, 2015 at KPCL (-37.2°C). Again, WRF was able to capture the events leading to the particularly cold December 2015 period. On December 27, the simulated minimum air temperature was -37.7°C at KPC_L and -37.8°C at KPC_U. The minimum daily values are warmer than those observed at KPC_U, but very similar to those observed at KPC_L. (Table 2).
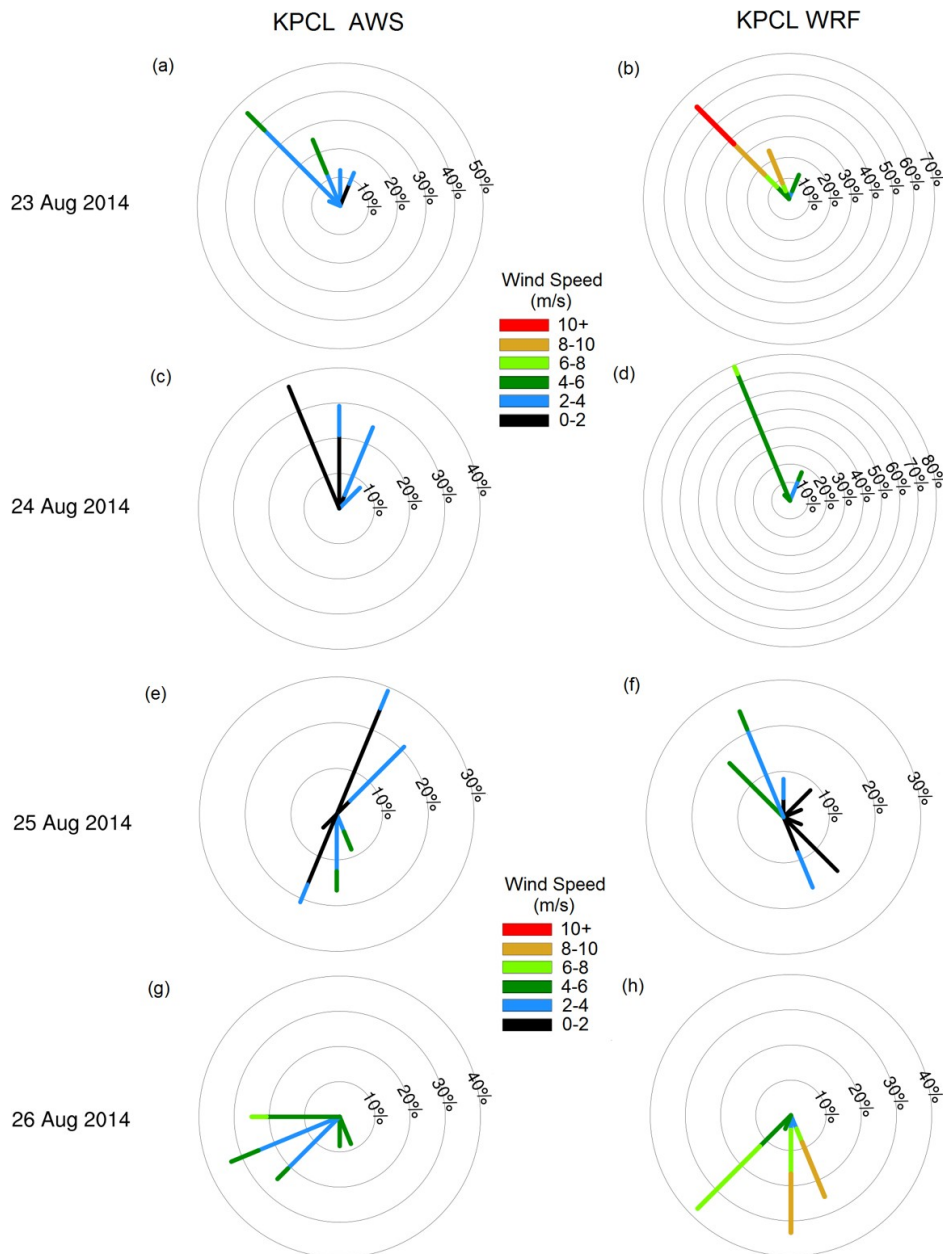
Figure 5: Wind speed (colour) and direction (lines) for August 23 to 26, 2014, from observations (left panel) and WRF (right panel) at KPC_L location. The circles (and therefore length of the spikes) represent the frequency of the particular wind direction, with the percentage of occurrence written on the circles.

4. Conclusions

Polar WRF has previously been extensively used in the Arctic (e.g Hines et al., 2011; Hines, & Bromwich, 2017; Wilson et al., 2011), including for Greenland (e.g DuVivier & Cassano., 2013; Turton et al., 2019a), for a number of applications. However, WRF runs have often been used for short case studies or performed at lower spatial resolution. This dataset provides high spatial and temporal resolution runs over multiple years (2014-2018) for an area of increased interest. Regardless

383 of the regular use of Polar WRF, it remains important to validate the model for specific locations,

384 especially when downscaling to very high resolutions.

385 Overall, the mean biases are small and statistically insignificant between the Polar WRF runs

386 and the PROMICE observations at both the lower and upper stations near 79°N glacier. The R^2

387 values are high for air temperature, humidity and wind speed, but less so for wind direction at

388 KPC_L. The wind direction is more variable in summer than in other months, and whilst WRF is able

389 to simulate the increased variability, large biases can arise due to inconsistent timing of wind direction

390 changes between WRF and observations over short periods of 24-hours or less. However, as WRF is

391 able to replicate the short-lived events and the predominant northwesterly winds of katabatic origin,

392 we can conclude that the NEGIS_WRF can be used for further studies of the near-surface meteorology

393 of the 79°N glacier. This dataset will be useful for many other applications in a number of fields

394 including the atmospheric and cryospheric sciences, and as input to hydrological, ice sheet and ocean

395 models, subject to appropriate validation.
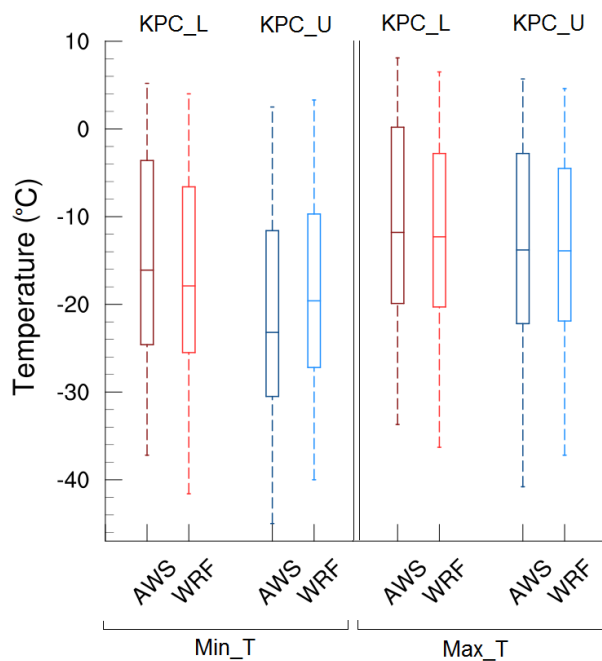
396

397

398 **Figure 6: Box plot representing the minimum (left) and maximum (right) daily temperature**

399 **values at KPC_L (red) and KPC_U (blue) locations, from both observations (darker colours)**

400 **and WRF (lighter colours).**

401

402 **5. Data Availability**

403 The atmospheric dataset, NEGIS_WRF resolves for the first time, the meteorological conditions over

404 the northeast region of Greenland (5km) and 79°N glacier region at the kilometre scale over a period

405 of five years (2014-2018). More than 50 variables are available (near-surface and on 60 atmospheric

406 levels) at up to hourly temporal resolution (for the 1 km domain), including meteorological and

radiative fields. Daily mean values for near-surface temperature (2m), specific humidity (2m), skin temperature, and U and V wind components (10m) are available online (Turton et al 2019b: doi.org/10.17605/OSF.IO/53E6Z) for the 1km and 5km domains from 2014-2018. As the output frequency from D01 (25km resolution) was once per day, the available values are instantaneous daily values at 00 UTC, as opposed to daily means. Furthermore, 4-D variables of temperature, humidity, U and V wind components, geopotential and pressure are available on model levels at the same frequency as the near-surface variables. For other variables, or more frequent output, please contact the lead author, and these can be made available. Due to the large amount of data, these are not stored online, but at the Regional Computation Centre Erlangen (RRZE) in Germany.

6. Author Contributions

JVT wrote the paper, ran the WRF model and evaluated it against the observations. TM and EC contributed to the research concept, discussion, optimisation of the simulations and manuscript refinement.

7. Competing Interests

The authors have no competing interests.

8. Acknowledgements

We thank Dirk van As from GEUS for his assistance with the PROMICE data and to Keith Hines for the Polar WRF code. The authors also thank two anonymous reviewers and Dr Yasuhiro Murayama for improving and editing our manuscript. This work was supported by the German Federal Ministry for Education and Research (BMBF) and forms part of the GROCE project (Greenland Ice Sheet/Ocean Interaction) (Grant 03F0778F). We acknowledge the High Performance Computing Centre (HPC) at the University of Erlangen-Nürnberg's Regional Computation Centre (RRZE), for their support and resources whilst running the Polar WRF simulations.

9. References

Banzon, V., Smith, T.M., Chin, T.M., Liu, C. and Hankins, W: A long-term record of blended satellite and in situ sea-surface temperature for climate monitoring, modelling and environmental studies, Earth Syst. Sci. Data, 8, 165-176. https://doi.org/10.5194/essd-8 165/2016, 2016.

Bennartz, R., Shupe, M. D., Turner, D. D., Walden, V. P., Steffen, K., Cox, C. J., … Pettersen, C: July 2012 Greenland melt extent enhanced by low-level liquid clouds, Nature, 496(7443), 83–86. https://doi.org/10.1038/nature12002, 2013.

Bowden, J.H., Nolte, C.G. and Otte, T.L: Simulating the impact of the large-scale circulation on the 2-m temperature and precipitation climatology. Clim. Dyn., 40, 1903-1920, https://doi.org/10.1007/s00382-012-1440-y, 2013.

444   Bromwich, D. H., Hines, K. M., and Bai, L: Development and testing of Polar Weather Research and

445   Forecasting model: 2. Arctic Ocean, J. of Geophys. Res., *114*(D8), D08122.

446   https://doi.org/10.1029/2008JD010300, 2009.

447   Chen, F and Dudhia, J: Coupling an advanced land surface-hydrology model with the Penn State-

448   NCAR MM5 modeling system. Part 1: Model implementation and sensitivity. Mon. Weather Rev.,

449   129, 569-585, https://doi.org/10.1175/15200493(2001)129<0569:CAALSH>2.0.CO;2, 2001.

450   Cho, H., Jun, S-Y., Ho, C-H. and McFarquhar, G: Simulations of winter Arctic clouds and associated

451   radiation fluces using different cloud microphysics schemes in the Polar WRF: Comparisons with

452   CloudSat, CALIPSO and CERES. JGR:Atmospheres, 125(2), e2019JD031413.

453   https://doi.org/10.1029/2019JD031413, 2020.

454   Dee, D. P., Uppala, S. M., Simmons, A. J., Berrisford, P., Poli, P., Kobayashi, S., … Vitart, F: The

455   ERA-Interim reanalysis: configuration and performance of the data assimilation system. Quart. J.

456   of the R Met. Soc., 137(656), 553–597, https://doi.org/10.1002/qj.828, 2011.

457   DuVivier, A. K., and Cassano, J. J: Evaluation of WRF Model Resolution on Simulated Mesoscale

458   Winds and Surface Fluxes near Greenland. Mon. Weather Rev., 141(3), 941–963.

459   https://doi.org/10.1175/MWR-D-12-00091.1, 2013.

460   ENVEO: Greenland Calving Front Dataset, 1990-2017, v3.0, Greenland Ice Sheet CCI, from

461   http://cryoportal.enveo.at, 2019.

462   European Space Agency Climate Change Initiative landuse product, available from

463   https://www.esalandcover-cci.org/, last accessed September 5 2019.

464   Fausto, R.S and van As, D: Programme for monitoring of the Greenland ice sheet (PROMICE):

465   Automatic weather station data. Version: v03, Dataset published via Geological Survey of

466   Denmark and Greenland. https://doi.org/10.22008/promice/data/aws, 2019.

467   Fettweis, X., Box, J. E., Agosta, C., Amory, C., Kittel, C., Lang, C., … Gallée, H: Reconstructions

468   of the 1900-2015 Greenland ice sheet surface mass balance using the regional climate MAR model.

469   The Cryosphere, 11(2), 1015–1033, https://doi.org/10.5194/tc-11-1015-2017, 2017.

470   Hines, K. M., and Bromwich, D. H: Development and Testing of Polar Weather Research and

471   Forecasting (WRF) Model. Part I: Greenland Ice Sheet Meteorology*, Mon. Weather Rev., 136(6),

472   1971–1989, https://doi.org/10.1175/2007MWR2112.1, 2008.

473   Hines, K. M., Bromwich, D. H., Bai, L.-S., Barlage, M., Slater, A. G., Hines, K. M., … Slater, A.

474   G: Development and Testing of Polar WRF. Part III: Arctic Land*, J. of Climate, 24(1), 26–48.

475   https://doi.org/10.1175/2010JCLI3460.1, 2011.

476   Hines, K. M., Bromwich, D. H., Bai, L., Bitz, C. M., Powers, J. G., Manning, K. W., …

477   Manning, K. W: Sea Ice Enhancements to Polar WRF*. Mon. Weather Rev., 143(6), 2363-

478   2385. https://doi.org/10.1175/MWR-D-14-00344.1, 2015.

479   Hines, K. M., and Bromwich, D. H: Simulation of Late Summer Arctic Clouds during ASCOS with

480   Polar WRF. Mon. Weather Rev., 145(2), 521–541. https://doi.org/10.1175/MWR D-16-0079.1, 2017.

481   Hochreuther, P, Friedrich Alexander Universtiy, Personal Communication, July 2019.

482   Hong, S.-Y., Noh, Y., Dudhia, J., Hong, S.-Y., Noh, Y., and Dudhia, J: A New Vertical Diffusion

483   Package with an Explicit Treatment of Entrainment Processes. Mon. Weather Rev., 134(9), 2318–

484   2341. https://doi.org/10.1175/MWR3199.1, 2006.

485   Howat, I. and Eddy, A: Multi-decadal retreat of Greenland's marine-terminating glaciers. J. of

486   Glaciology, 57(203), 389-396. Doi:10.3189/002214311796905631, 2011.

487   Janjić, Z. I: The Step-Mountain Eta Coordinate Model: Further Developments of the Convection,

488   Viscous Sublayer, and Turbulence Closure Schemes. Mon. Weather Rev.,122(5),927–945,

489   https://doi.org/10.1175/15200493(1994)122<0927:TSMECM>2.0.CO;2, 1994.

490   Joughin, I., Smith, B. E., Howat, I. M., Scambos, T., and Moon, T: Greenland flow variability from

491   ice-sheet-wide velocity mapping. *Journal of Glaciology*, *56*(197), 415–430,

492   https://doi.org/10.3189/002214310792447734, 2010.

493   Kain, J. S: The Kain–Fritsch Convective Parameterization: An Update. J. of App. Met.,   43(1),

494   170–181.https://doi.org/10.1175/1520-0450(2004)043<0170:TKCPAU>2.0.CO;2, 2004.

495   Khan, S. A., Kjær, K. H., Bevis, M., Bamber, J. L., Wahr, J., Kjeldsen, K. K., … Muresan, I. S:

496   Sustained mass loss of the northeast Greenland ice sheet triggered by regional warming. Nature

497   Climate Change, 4(4), 292–299. https://doi.org/10.1038/nclimate2161, 2014.

498   Kuipers Munneke, P., Smeets, C. J. P. P., Reijmer, C. H., Oerlemans, J., van de Wal, R. S. W., and

499   van den Broeke, M. R: The K-transect on the western Greenland Ice Sheet: Surface energy balance

500   (2003–2016).   Arctic,   Antarctic,   and   Alpine   Res.,   50(1),   e1420952.

501   https://doi.org/10.1080/15230430.2017.1420952, 2018.

502   Lachlan-Cope, T., Listowski, C., and O'Shea, S: The microphysics of clouds over the Antarctic

503   Peninsula - Part 1: Observations, Atmos. Chem. Phys., 16(24), 15605–15617.

504   https://doi.org/10.5194/acp-16-15605-2016, 2016.

505   Larsen, N. K., Levy, L. B., Carlson, A. E., Buizert, C., Olsen, J., Strunk, A., … Skov, D. S:

506   Instability of the Northeast Greenland Ice Stream over the last 45,000 years, Nature Comms, 9(1),

507   1872. https://doi.org/10.1038/s41467- 018-04312-7, 2018.

508   Leeson, A. A., Eastoe, E., and Fettweis, X: Extreme temperature events on Greenland in

509   observations and the MAR regional climate model, The Cryosphere, 12(3), 1091–1102.

510   https://doi.org/10.5194/tc-12-1091-2018, 2018.

511   Listowski, C., and Lachlan-Cope, T: The microphysics of clouds over the Antarctic Peninsula Part 2:

512   modelling aspects within Polar WRF, Atmos. Chem. Phys, 17(17),   10195-10221.

513   https://doi.org/10.5194/acp-17-10195- 201717, 2017.

Lo, J.C-F., Yang, Z-L. and Pielke Sr, R.A: Assessment of three dynamical climate downscaling methods using the Weather Research and Forecasting (WRF) model, JGR: Atmospheres. 113, D09112, https://doi.org/10.1029/2007JD009216, 2008.

Mayer, C., Schaffer, J., Hattermann, T., Floricioiu, D., Krieger, L., Dodd, P. A., … Schannwell, C: Large ice loss variability at Nioghalvfjerdsfjorden Glacier, Northeast Greenland, Nature Comms, 9(1), 2768. https://doi.org/10.1038/s41467-01805180-x, 2018.

Mernild, S. H., Liston, G. E., van As, D., Hasholt, B., and Yde, J. C: High-resolution ice sheet surface mass-balance and spatiotemporal runoff simulations: Kangerlussuaq, west Greenland, Arctic, Antarctic, and Alpine Res., 50(1) S100008. https://doi.org/10.1080/15230430.2017.1415856, 2017.

Mottram, R., Boberg, F., Langen, P., Yang, S., Rodehacke, C., Christensen, J., and Madsen, M: Surface mass balance of the Greenland ice sheet in the regional climate model HIRHAM5: Present state and future prospects, Low Temp. Sci., *75*, 105-115, 2017a.

Mottram, R., Nielsen, K.P., Gleeson, E., Yang, X: Modelling Glaciers in the HARMONIE-AROME NWP model, Adv. Sci. Res., 14, 323–334, https://doi.org/10.5194/asr-14-323-2017, 2017b.

Mouginot, J., Rignot, E., Scheuchl, B., Fenty, I., Khazendar, A., Morlighem, M., … Paden, J: Fast retreat of Zachariæ Isstrøm, northeast Greenland. *Science*, *350*(6266), 1357-1361, https://doi.org/10.1126/SCIENCE.AAC7111, 2015.

Münchow, A., Schaffer, J. and Kanzow, T: Ocean circulation connecting Fram Strait to Glaciers off North-East Greenland: Mean flows, topographic Rossby waves, and their forcing. J. Phys. Oceanography, 50, 509-530, https://doi.org/10.1175/JPO-D-19-0085.1, 2020.

Niwano, M., Aoki, T., Hashimoto, A., Matoba, S., Yamaguchi, S., Tanikawa, T., Fujita, K., Tsushima, A., Iizuka, Y., Shimada, R., and Hori, M: NHM–SMAP: spatially and temporally high resolution nonhydrostatic atmospheric model coupled with detailed snow process model for Greenland Ice Sheet, The Cryosphere, 12, 635–655, https://doi.org/10.5194/tc-12-635-2018, 2018.

Noël, B., van de Berg, W. J., Machguth, H., Lhermitte, S., Howat, I., Fettweis, X., and van den Broeke, M. R: A daily, 1 km resolution data set of downscaled Greenland ice sheet surface mass balance (1958–2015). The Cryosphere, 10(5), 2361–2377, https://doi.org/10.5194/tc-10-2361-2016, 2016.

Otte, T.L., Nolte, C.G., Otte, M.J. and Bowden, J.H: Does Nudging Squelch the Extremes in Regional climate modeling? J. of Climate*,* 25, 7046-7066, https://doi.org/10.1175/JCLID-12-00048.1, 2012.

Pal, S., Change, H-I., Castro, C.L. and Dominguez, F: Credibility of convection-permitting modeling to improve seasonal precipitation forecasting in the southwestern United States. Frontiers Earth Sci.,. 7, 11. https://doi.org/10.3389/feart.2019.00011, 2019.

550 Pedersen, S.H., Tamstorf, M.P., Abermann, J., Westergaard-Nielsen, A., Lund, M… Schmidt,
551 N.M: Spatiotemporal characteristics of seasonal snow cover in Northeast Greenland from in situ
552 observations. Arctic, Antarctic and Alpine Res., 48 (4), 653-671.
553 https://doi.org/10.1657/AAAR0016-028, 2016.

554 Polar Weather Research and Forecasting Model, developed by Ohio State University, available
555 from: http://polarmet.osu.edu/PWRF/, last accessed: July 29 2019.

556 Powers, J. G., Klemp, J. B., Skamarock, W. C., Davis, C. A., Dudhia, J., Gill, D. O., … Duda, M.
557 G: The Weather Research and Forecasting Model: Overview, System Efforts, andFuture
558 Directions, Bull. American Met. Soc, 98(8), 1717–1737. https://doi.org/10.1175/BAMS-D-15-
559 00308.1, 2017.

560 Rignot, E., Fenty, I., Xu, Y., Cai, C., and Kemp, C: Undercutting of marine-terminating glaciers in
561 West Greenland, Geophys. Res. Letters, 42(14), 5909–5917, https://doi.org/10.1002/2015GL064236,
562 2015.

563 Schaffer, J., von Appen, W.-J., Dodd, P. A., Hofstede, C., Mayer, C., de Steur, L., and Kanzow,
564 T: Warm water pathways toward Nioghalvfjerdsfjorden Glacier, Northeast Greenland, J. Geophys.
565 Res: Oceans, 122(5), 4004–4020, https://doi.org/10.1002/2016JC012462, 2017a.

566 Sea Surface Temperature and Sea Ice Concentration Data, available from
567 https://rda.ucar.edu/datasets/ds277.7/, last accessed July 29 2019, doi:10.5065/EMOT-ID34

568 Shepherd, A., Ivins, E., Rignot, E… Wuite, J: Mass balance of the Greenland Ice Sheet from 1992 to
569 2018, Nature, 579, 233-239, https://doi.org/10.1038/s41586-019-1855-2, 2020.

570 Skamarock, W. C., and Klemp, J. B: A time-split nonhydrostatic atmospheric model for weather
571 research and forecasting applications. J. Computational Phys, 227(7), 3465–3485.
572 https://doi.org/10.1016/j.jcp.2007.01.037, 2008.

573 Tedesco, M., Fettweis, X., Mote, T., Wahr, J., Alexander, P., Box, J. E., and Wouters, B: Evidence
574 and analysis of 2012 Greenland records from spaceborne observations, a regional climate model
575 and reanalysis data, The Cryosphere, 7(2), 615–630, https://doi.org/10.5194/tc-7-615-2013, 2013.

576 Turton, J. V., Mölg, T. & Van As, D: Atmospheric Processes and Climatological Characteristics
577 of the 79N Glacier (Northeast Greenland), Mon. Weather Rev., 147(4), 1375–1394.
578 https://doi.org/10.1175/MWR-D-18-0366.1, 2019a.

579 Turton, J. V., Mölg, T and Collier, E: NEGIS_WRF model output, Open Science Framework
580 Repository, last accessed October 1 2019, doi: /10.17605/OSF.IO/53E6Z, 2019b.

581 Van As, D., Boggild, C.E., Nielsen, S., Ahlstrom, A.P., Fausto, R.S., Podlech, S. and Andersen, M.L:
582 Climatology and ablation at the South Greenland ice sheet margin from automatic weather station
583 observations. The Cryosphere Discussions. 3, 117-158, https://doi.org/10.5194/tcd-3-117-2009, 2009.

584 van As, D., & Fausto, R: Programme for Monitoring of the Greenland Ice Sheet (PROMICE): first
585 temperature and ablation records. Geolog. Survey Denmark Greenland Bulletin, 23, 73–76, 2011.

586   van den Broeke, M., Box, J., Fettweis, X., Hanna, E., Noël, B., Tedesco, M., … van Kampenhout,

587   L: Greenland Ice Sheet Surface Mass Loss: Recent Developments in Observation and   Modeling.

588   Current Climate Change Rep, 3(4), 345–356, https://doi.org/10.1007/s40641-017-0084-8, 2017.

589   Wang, C., Graham, R.M., Wang, K., Gerland, S. and Granskog, M.A: Comparison of ERA5 and

590   ERA-Interim near surface air temperature, snowfall and precipitation over Arctic sea ice: effects on

591   sea ice thermodynamics and evolution. The Cryosphere, 13, 1661-1679, https://doi.org/10.5194/tc-

592   13-1661-2019, 2019.

593   Weather Research and Forecasting Model, developed by the National Centre for Atmospheric

594   Research   (NCAR).   Available   from: https://www.mmm.ucar.edu/weather-research-and

595   forecasting-model, last accessed: October 1 2019.

596   Wilson, A. B., Bromwich, D. H., & Hines, K. M: Evaluation of Polar WRF forecasts on the Arctic

597   System Reanalysis domain: Surface and upper air analysis. *J. Geophys. Res.*, *116*(D11), D11112.

598   https://doi.org/10.1029/2010JD015013, 2011.

599